

Wave Scattering by 2D Smooth Topographical Elastic Deformations Caused by a Point Blast Source

Paulo Santos, Julieta António, António Tadeu¹

Abstract: This paper presents the three-dimensional scattering field obtained when 2D smooth topographical deformations are subjected to a dilatational point load placed at some point in the medium. The solution is formulated using boundary elements for a wide range of frequencies and spatially harmonic line loads, which are then used to obtain time series by means of (fast) inverse Fourier transforms into space-time. The topographical surface is modeled with a number of boundary elements, defined according to the excitation frequency of the harmonic source, and in such a way that the free surface can be discretized along a sufficient distance to fully reproduce the responses at the receivers in the time window considered ($T = 1/\Delta f$).

Simulation analyses utilizing this idealized model are used to study the alteration of the wave scattering generated by the half-space, when the free surface is changed to simulate a ridge or a valley deformation. The amplitude of the wavefield in the frequency vs axial-wavenumber domain is presented to allow the recognition, identification, and physical interpretation of the variation of the wavefield.

keyword: boundary elements, topographic deformations, point blast source, seismic wave amplification

1 Introduction

Surface topographical deformations produce site effects, leading to seismic signal amplification, and these can be significant over a large frequency domain [Davis and West (1973); Griffiths and Bollinger (1979); Bard and Tucker (1985)]. The prediction of the ground movement in the vicinity of different topographic deformations has occupied many researchers for years. Some of the first analytical studies on wave diffraction and scattering looked at wave motion and reverberations in alluvial basins of regular shape [Trifunac (1971); Trifunac (1973); Wong and Trifunac (1974); Lee and Cao (1989); Todorovska and Lee (1990), (1991)], and the wave scattering induced by cavities [Lee (1977); Datta and Shah (1982); Lee (1988); Lee and Karl (1992)]. More recently, semi-analytical methods have been used to study wave diffraction caused by geological irregularities of arbitrary shape within globally homogeneous media [Sanchez-Sesma (1983); Moeen-Vaziri and Trifunac (1988); Lee and Wu (1994)]. By contrast, the application of purely numerical methods (i.e. finite elements or

differences combined with boundaries) have mostly been employed in situations where the response is required only within localised irregular domains, such as soil-structure interaction problems [Waas (1972); Lysmer, Udaka, Seed, and Hwang (1974); Kausel (1974)]. Techniques based on representation theorems have also been developed to model topographic effects: the direct boundary element method (BEM) [Wong and Jennings (1975); Zhang and Chopra (1991)], the indirect boundary element method (IBEM) [Sánchez-Sesma and Rosenblueth (1979); Wong (1982); Luco, Wong, and De Barros (1990); Sánchez-Sesma and Campillo (1991), (1993)] and combinations of integral representations with discrete wave number expansions of Green's functions [Bouchon (1985); Kawase (1988); Pei and Papageorgiou (1993)]. Discrete methods have also occasionally been used to model large alluvial basins, but only in plane-strain [Ohtsuki and Harumi (1983)]. Finally, hybrid methods involving a combination of finite elements to model the interior domain containing the inhomogeneities and semi-analytical representations for the exterior domain have been used [Shah, Wong, and Datta (1982)]. The above methods have been reviewed in detail by Sánchez-Sesma (1987).

These methods have largely been employed in cases where a two-dimensional (2D) solution is wanted. However, site observations appear to indicate amplification that is both higher and more broadband than predicted by numerical simulations [Bard and Tucker (1985); Geli, Bard, and Jullien (1988)]. The need to extend the numerical simulation to more realistic models, taking into account the three-dimensional character of real topographical deformations, is recognized. If the full scattering wave field, generated by sources placed in the presence of three-dimensional (3D) propagation media, is evaluated, then the numerical calculations are very costly in terms of computer effort.

If the medium is 2D and the dynamic source 3D (such as a point load), the model is often termed a two-and-a-half-dimensional problem (2-1/2-D) its solution becomes much simpler. Solutions for such problems involve a two spatial Fourier transform in the direction in which the geometry does not vary. A sequence of 2D problems with different spatial wavenumbers, k_z , must first be solved, and then the inverse Fourier transform is used to synthesize the 3D field.

The 2-1/2-D wave equation for inclusions such as the circular cylinder can be separated, and so their solution can be

¹ Dep. of Civil Eng., University of Coimbra, Portugal

known in closed form. The solution is harder to determine for inclusions with irregular cross-sections. In these cases, the Boundary Element Method (BEM) may be the best tool, especially if the solution needs to satisfy the far field conditions required if the inclusions are buried in an unbounded or half-space elastic medium. Zhang and Chopra (1991) presented a BEM formulation to determine the three-dimensional seismic response of an infinitely long canyon of arbitrary cross-section in a homogeneous visco-elastic half-space. The dynamic excitation was represented by Rayleigh surface waves or plane body waves approaching the half-space from any direction. In their formulation, the three-dimensional boundary integral equation is reduced to a set of two-dimensional problems by means of Fourier transforms of the three dimensional Green's functions along the canyon axis. The required half-space surface discretization was performed on both sides of the canyon over a distance of at least twice the shear wavelength using equal linear boundary elements. The element size on the canyon surface was kept to less than one-fifth of the shear wavelength. The accuracy of the solution has been verified by comparison with previous solutions for the limited cases of two-dimensional response and three-dimensional response results for infinitely-long regular canyons provided by the indirect boundary method [Luco, Wong, and De Barros (1990)], when the medium is excited by a single harmonic plane source. This work also includes the comparison of the 2-1/2-D solution with the solution of a finite-length canyon provided by a fully three-dimensional boundary element method. This shows that the finiteness of the canyon has only a small effect on the displacements that are a long way from the ends of the canyon. Later, Pedersen, Sánchez-Sesma, and Campillo (1994) also studied the three dimensional seismic response of two-dimensional topographies to plane waves with an azimuth ψ , relative to the structure, and an incidence θ , relative to the vertical axis. They used the indirect boundary element method (IBEM), using the Green's functions for a harmonic point force moving along the axis of the topography in a full space. Pedersen, Sánchez-Sesma, and Campillo (1994) presented scattering results in the frequency and time domains for topographies of simple geometry, namely, a semi-circular canyon and a semi-circular ridge, when subjected to incident plane waves. The required numerical equations were defined assuming the surface topography to be divided into a number of segments, each with a constant force distribution. The number of segments was variable with frequency, allowing the existence of five segments per wavelength. Their results showed that the spectral amplitude of the seismic response in the cases of the semi-circular canyon or of the semi-ridge are dominated by the scattering generated by the edges of the canyon or of the ridge. The total scattered wave field presented a complicated pattern of amplification and deamplification, which does not seem to change to any great extent when the incident plane waves arrive outside the symmetry axis of the topography.

Stamos and Beskos (1996) presented a special direct bound-

ary element method to describe the 3D dynamic response of long lined tunnels with a uniform cross-section, buried in an elastic or visco-elastic half-space, and subjected to plane harmonic waves propagating in arbitrary directions. The problem is reduced to a two-dimensional one by a coordinate transformation and appropriate integration of the full space dynamic fundamental solution along the direction of the tunnel axis. Quadratic isoparametric line boundary elements are used, and the solutions compared with other methods.

In our work, the three-dimensional wave scattering in the vicinity of two dimensional topographies is addressed again using the BEM. The problem is similar to the one solved first by Zhang and Chopra and then by Pedersen et al, but here, the medium is illuminated by a dilatational point load (blast load) and the surface deformation is assumed to be a smooth canyon or a smooth ridge, in an attempt to extend the numerical simulation to more realistic models. The required half-space surface discretization is extended as expected along a finite length, although in this paper, smaller elements are placed in the vicinity of the axis deformation.

The solution at each frequency is given in terms of waves with varying wavenumber, k_z , (where z is the direction in which the geometry does not vary), using the appropriated Green's functions [Sánchez-Sesma and Campillo (1991), Tadeu and Kausel (2000)]. This is then Fourier transformed into the spatial domain. To find the wavenumber transform in discrete form, it is assumed that an infinite number of virtual point sources are equally spaced along the z axis, far enough apart to prevent spatial contamination [Bouchon and Aki (1977)]. The analyses utilize complex frequencies, moving down the frequency axis, in the complex plane. Thus, the neighboring fictitious sources can only exert a very slight influence [Phinney (1965)]. No claim is made here for theoretical or computational BEM innovation.

The rest of this paper explains briefly the BEM method and its validation. Then, this model is used for simulation analyses to investigate three-dimensional wave propagation in the vicinity of a flat half-space, a smooth canyon or a smooth ridge excited by a point load. Results are obtained in the frequency and in the time domains, in particular for the different apparent wave velocities along the z axis, for a quantitative study of the 3D effects of the scattering.

2 Problem formulation

Consider an infinitely long, cylindrical, irregular cavity buried in a uniform elastic medium (see Fig. 1) and subjected to a harmonic dilatational point source at position $(x_0, 0, 0)$, oscillating with a frequency Ω . The incident field can be expressed by means of the now classical dilatational potential ϕ

$$\phi_{inc} = \frac{Ae^{i\frac{\omega}{\alpha}(\alpha - \sqrt{(x-x_0)^2 + y^2 + z^2})}}{\sqrt{(x-x_0)^2 + y^2 + z^2}} \quad (1)$$

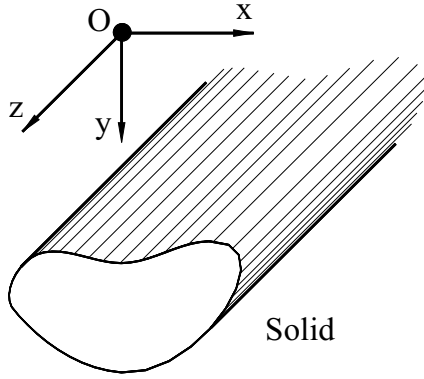


Figure 1 : Geometry of the problem.

where the subscript *inc* denotes the incident field, A is the wave amplitude, α is the compressional wave velocity of the medium, and $i = \sqrt{-1}$.

Defining the effective wavenumbers

$$k_\alpha = \sqrt{\frac{\omega^2}{\alpha^2} - k_z^2} \quad \text{Im } k_\alpha < 0 \quad (2)$$

by means of the axial wavenumber k_z , and Fourier-transforming Eq. 1 in the z direction, we get

$$\hat{\phi}_{inc}(\omega, x, y, k_z) = \frac{-iA}{2} H_0^{(2)} \left(k_\alpha \sqrt{(x-x_0)^2 + y^2} \right) \quad (3)$$

in which the $H_n^{(2)}(\dots)$ are second kind Hankel functions of order n .

When we take an infinite number of virtual point sources, equally spaced along the z direction at a sufficient distance, L , from each other to avoid spatial contamination [Bouchon and Aki (1977)], the incident field may be written as

$$\phi_{inc}(\omega, x, y, z) = \frac{2\pi}{L} \sum_{m=-\infty}^{\infty} \hat{\phi}_{inc}(\omega, x, y, k_z) e^{-ik_{zm}z} \quad (4)$$

with $k_{zm} = 2\pi/Lm$. This equation converges and can be approximated by a finite sum of terms.

3 Boundary element formulation

3.1 Cylindrical cavity

The 3D field generated by a cylindrical cavity subjected to spatially sinusoidal harmonic line loads (defined by Eq. 3) is found by means of the Boundary Element Method (BEM). Since the basic equations used when applying boundary elements to wave propagation are widely known [Manolis (1988); Banerjee (1994)], only a brief explanation of the method to be applied in the frequency domain, is presented.

The boundary integral equations can be constructed using the dynamic reciprocal theorem, through which, in the absence of distributed loads and in the presence of virtual point loads, $\delta(\mathbf{x} - \mathbf{x}_0)$, the following equation is defined,

$$c_{ij}u_j(\mathbf{x}_0, \omega) = \int_C t_i(\mathbf{x}, \nu, \omega) G_{ij}(\mathbf{x}, \mathbf{x}_0, \omega) ds - \int_C H_{ij}(\mathbf{x}, \nu, \mathbf{x}_0, \omega) u_j(\mathbf{x}, \omega) ds \quad (5)$$

In this equation $i, j = 1, 2$ stands for the normal and tangential directions relative to the cavity surface, respectively, while $i, j = 3$ refers to the z direction. $G_{ij}(\mathbf{x}, \mathbf{x}_0, \omega)$ and $H_{ij}(\mathbf{x}, \nu, \mathbf{x}_0, \omega)$ are the displacements and tractions in the direction j at \mathbf{x} (on the boundary C) as a result of a unit point force in the direction i at \mathbf{x}_0 (the source). The vector ν is the unit outward normal at the boundary, while c_{ij} is a constant, depending on the local geometry of the boundary. For a smooth boundary, c_{ij} is equal to $\delta_{ij}/2$, where δ_{ij} is the Kronecker's delta.

Expressions for the tensions may be obtained from the two-and-a-half dimensional fundamental solution (Green's functions), by taking partial derivatives to deduce the strains and then applying Hooke's law to find the stresses. The displacement and stress functions, in Cartesian co-ordinates, which apply to the present problem, are listed in Tadeu and Kausel (2000). These stress fields are conveniently transformed into the normal, tangential and z local co-ordinate system at each element by equilibrium relations. The boundary conditions at the boundary of a cavity prescribe null tractions, leading to the simplified form of Eq. 5,

$$c_{ij}u_j(\mathbf{x}_0, \omega) = - \int_C H_{ij}(\mathbf{x}, \nu, \mathbf{x}_0, \omega) u_j(\mathbf{x}, \omega) ds \quad (6)$$

The evaluation of this integral for an arbitrary cross section requires the discretization of both the boundary and boundary values. If N boundary elements are used and the nodal displacements are assumed to be constant within each element, and equal to the value at the associated nodal point, Eq. 6 changes to

$$c_{ij}u_j^k = - \sum_{n=1}^N H_{ij}^{kn} u_j^n \quad (7)$$

In this equation, k is the element number at the point where the virtual load is applied, u_j^n is the boundary values in element n , and H_{ij}^{kn} is the element integrals

$$H_{ij}^{kn} = \int_{C_n} H_{ij}(\mathbf{x}, \nu_n \mathbf{x}_k, \omega) ds \quad (8)$$

in which ν_n is the unit outward normal for n^{th} boundary segment C_n .

By successively applying the virtual load to each node on the boundary, a system of linear equations relating nodal forces

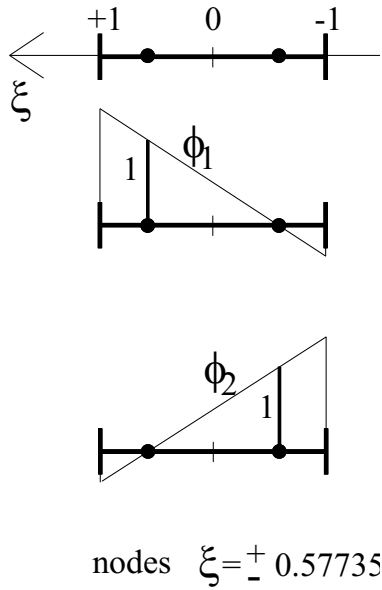


Figure 2 : Discontinuous linear boundary elements. Interpolating functions and nodal points position.

and nodal displacements is obtained, and these can be solved for the nodal displacements.

If an incident wave strikes the cavity, Eq. 6 changes to

$$c_{ij}u_j(\mathbf{x}_0, \omega) = - \int_C H_{ij}(\mathbf{x}, \nu, \mathbf{x}_0, \omega) u_j(\mathbf{x}, \omega) ds + u_j^{inc}(\mathbf{x}_0, \omega) \quad (9)$$

In this equation the incident field is obtained by taking partial derivatives of Eq. 3 to deduce displacements along x , y and z , and then applying equilibrium relations to obtain the normal and tangential displacements along the boundary.

If the displacements and tractions are allowed to vary linearly within the boundary elements, the required integrals of Eq. 8 change to

$$H_{ij}^{kn} = \int_{C_n} \phi H_{ij}(\mathbf{x}_n, \nu_n \mathbf{x}_k, \omega) ds \quad (10)$$

where ϕ are the linear interpolation functions.

The displacement and stress variations within a boundary element are defined in terms of the nodal values. The traction discontinuity at the corner between two boundary elements is handled by means of discontinuous boundary elements. Thus, the nodes that would meet at the corner are moved inside [Brebbia (1984)]. Figure 2 displays the interpolation functions used and the position of the nodal points.

In this work, the required integrations in Eq. 10 are performed using Gaussian quadrature when the element to be integrated is not the loaded element. For the loaded element, the exist-

ing singular integrands are carried out in closed form [Tadeu (1999a), (1999b)].

3.1.1 Validation of the BEM Algorithm

The BEM algorithm was implemented and validated by applying it to a cylindrical circular cavity, placed in a homogeneous elastic medium, subjected to a dilatational point load applied at point O , as in Fig. 3a, for which the solution is known in closed form and described in Pao and Mow (1973).

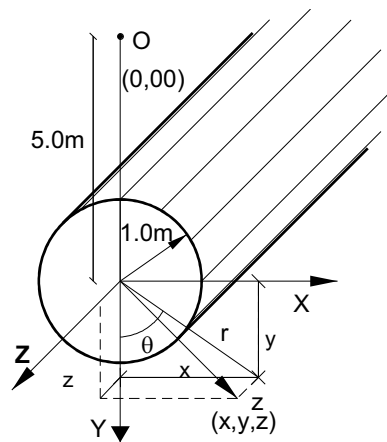
The response is calculated over a fine vertical grid plane, placed perpendicular to the z axis. Figure 3c gives the analytical scattered z displacement field computed when a harmonic pressure load of 2450 Hz is excited. The difference in the response obtained using the BEM - the error - when the inclusion is modeled with 17 and 52 linear boundary elements, is displayed in Fig. 3d and 3e, respectively.

In the present example, the ratio between the wavelength of the dilatational waves to the length of boundary elements varies between 3 (17 boundary elements) and 9.0 (52 boundary elements). The BEM accuracy improves as shorter boundary elements are used to model the response, as anticipated.

3.2 Surface topography

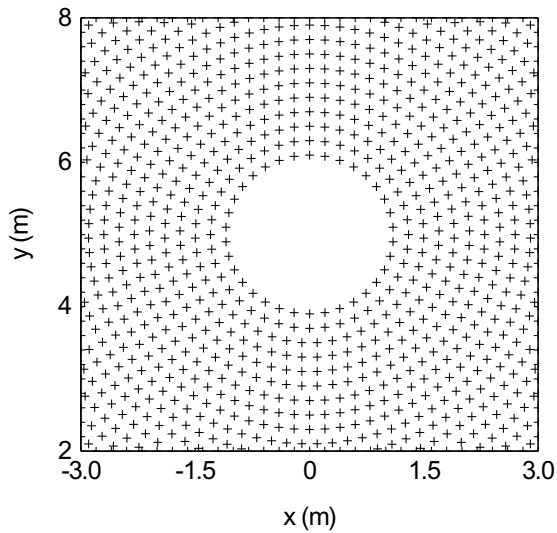
The surface topography can be described as a cavity of infinite size. So, the equations developed for the cylindrical cavity (Eq. 5), above, can be used to calculate its solution. The use of complex frequencies together with the geometrical damping of the response with distance makes the full discretization of the infinite surface unnecessary. Boundary elements are only required to the extent that they make a significant contribution to the response. If solutions are required in the time domain, the contribution to the response behind the time window, defined by the frequency step of the analysis, $T = 2\pi/\Delta\omega$, need not be taken into account. Hence, the boundary elements are distributed along the surface up to a spatial distance (L_{dist}) from the receivers, given by $L_{dist} = \alpha T$. This gives a discretized surface with a length $2L_{dist} + 2a$, where $2a$ is the length of the segment occupied by the receivers. Many simulations were performed to study how varying the size of boundary elements affects the accuracy of the response. The performance was found to be better when smaller elements were placed in the vicinity of the receivers. The authors of this paper suggest that boundary elements of varying size should be placed along the surface, with the shorter elements being used nearer to the center of the surface boundary discretization, thereby reducing computational cost.

Figure 4 illustrates the scheme used in this work to determine the placement and size of the boundary elements. It makes use of a geometrical construction, by which an auxiliary circular arc is divided into equal segments according to a previously defined ratio between the wavelength of the dilatational waves and the length of boundary elements.

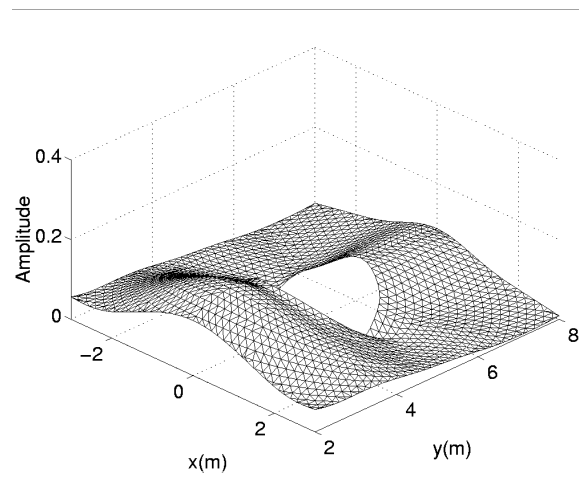


$\beta = 265 \text{ m/s}$
 $\rho = 2140 \text{ kg/m}^3$
 $\alpha = 4208 \text{ m/s}$

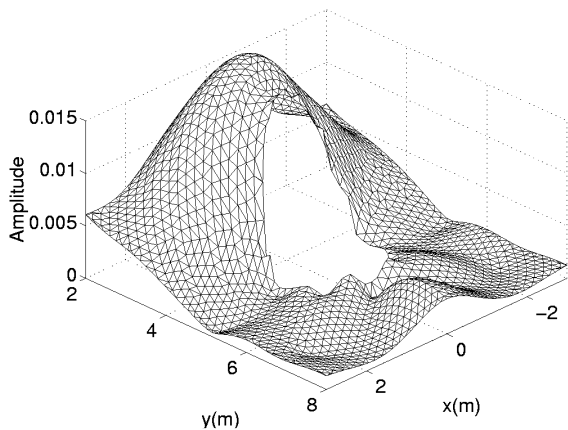
(a) Geometry



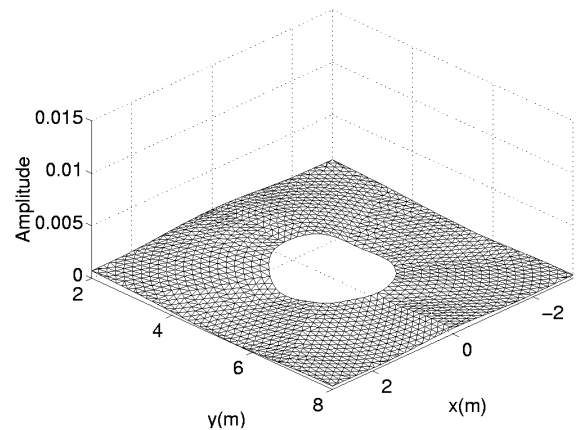
(b) Receivers grid



(c) Analytical x displacement



(d) BEM error – 17 elements



(e) BEM error – 52 elements

Figure 3 : Circular problem validation.

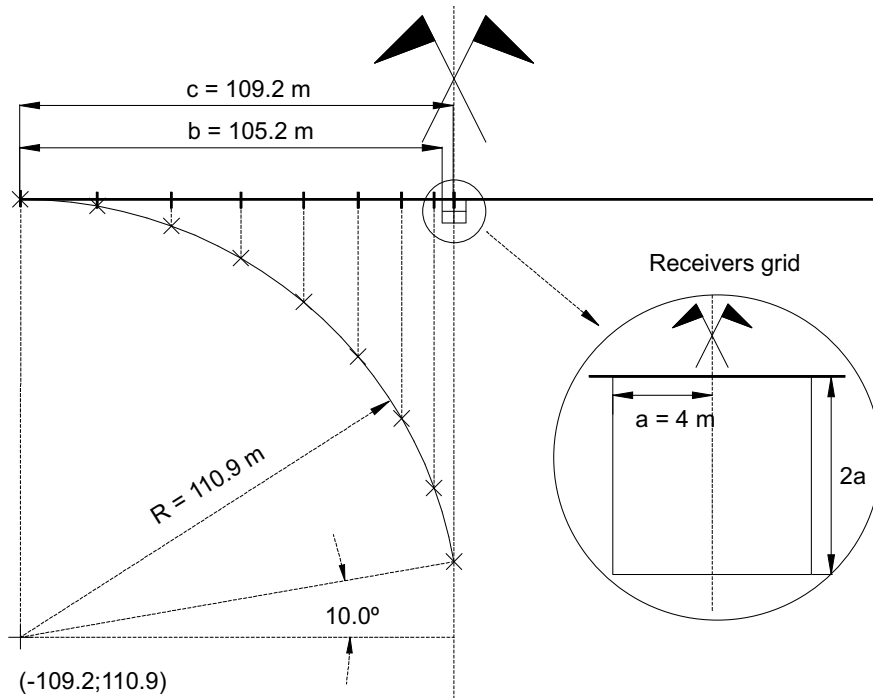


Figure 4 : Boundary elements distribution ($f = 100 \text{ Hz} - \Delta f = 40 \text{ Hz}$).

The boundary elements are then defined on the topographic surface by the vertical projection of these segments. The radius of the required circular arc (R) is bigger than $(2L_{dist} + 2a)/2$ and is placed tangent to the topographic surface at its boundary discretization end, avoiding the existence of unduly small boundary elements. In this work R is assumed to be $[(2L_{dist} + 2a)/2] / \cos 10^\circ$.

3.2.1 Validation of the BEM algorithm

The BEM algorithm was implemented and validated by applying it to a flat half-space, subjected to a dilatational line load placed at $x = 0.0 \text{ m}$ and $y = 0.6 \text{ m}$, as in Fig. 5a, for which the solution is known in closed form and described in Kawase (1988).

Figure 5 shows the horizontal displacement field, over a fine vertical grid plane, placed perpendicular to the z axis, computed when a harmonic pressure line load of 100 Hz is excited. Figure 5b displays the response given by the closed form solution. The difference in the response obtained using the BEM (the error) is presented for a ratio between the wavelength of the dilatational waves and the length of boundary elements equal to 10, when 122 linear boundary elements are used. Figure 5c presents the error when evenly-spaced boundary elements are used along the surface boundary. Figure 5d shows the error when the length of the boundary elements is varied according to the method described above (see Fig. 4). It can be concluded that, for the same computational cost, the

BEM accuracy improves with the use of shorter boundary elements as we move to the center of the surface discretization.

4 Results in space-time

A numerical fast Fourier transform in k_z gives the displacements in the spatial-temporal domain, taking a source whose temporal variation is given by a Ricker wavelet, as defined below. The Ricker wavelet has the advantage of decaying rapidly, in both time and frequency, which both reduces computational effort, and allows the computed time series and synthetic waveforms to be interpreted more easily.

The Ricker wavelet function is given by

$$u(\tau) = A (1 - 2\tau^2) e^{-\tau^2} \tag{11}$$

where A is the amplitude, $\tau = (t - t_s)/t_0$ and t denotes time; t_s is the time when the maximum occurs, while πt_0 is the characteristic (dominant) period of the wavelet. Its Fourier transform is

$$U(\omega) = A [2\sqrt{\pi} t_0 e^{-i\omega t_s}] \Omega^2 e^{-\Omega^2} \tag{12}$$

in which $\Omega = \omega t_0/2$.

The Fourier transformations are achieved by discrete summations over wavenumbers and frequencies, which is mathematically the same as adding periodic sources at spatial intervals $L = 2\pi/\Delta k_z$ (in the z -axis), and temporal intervals $T = 2\pi/\Delta\omega$,

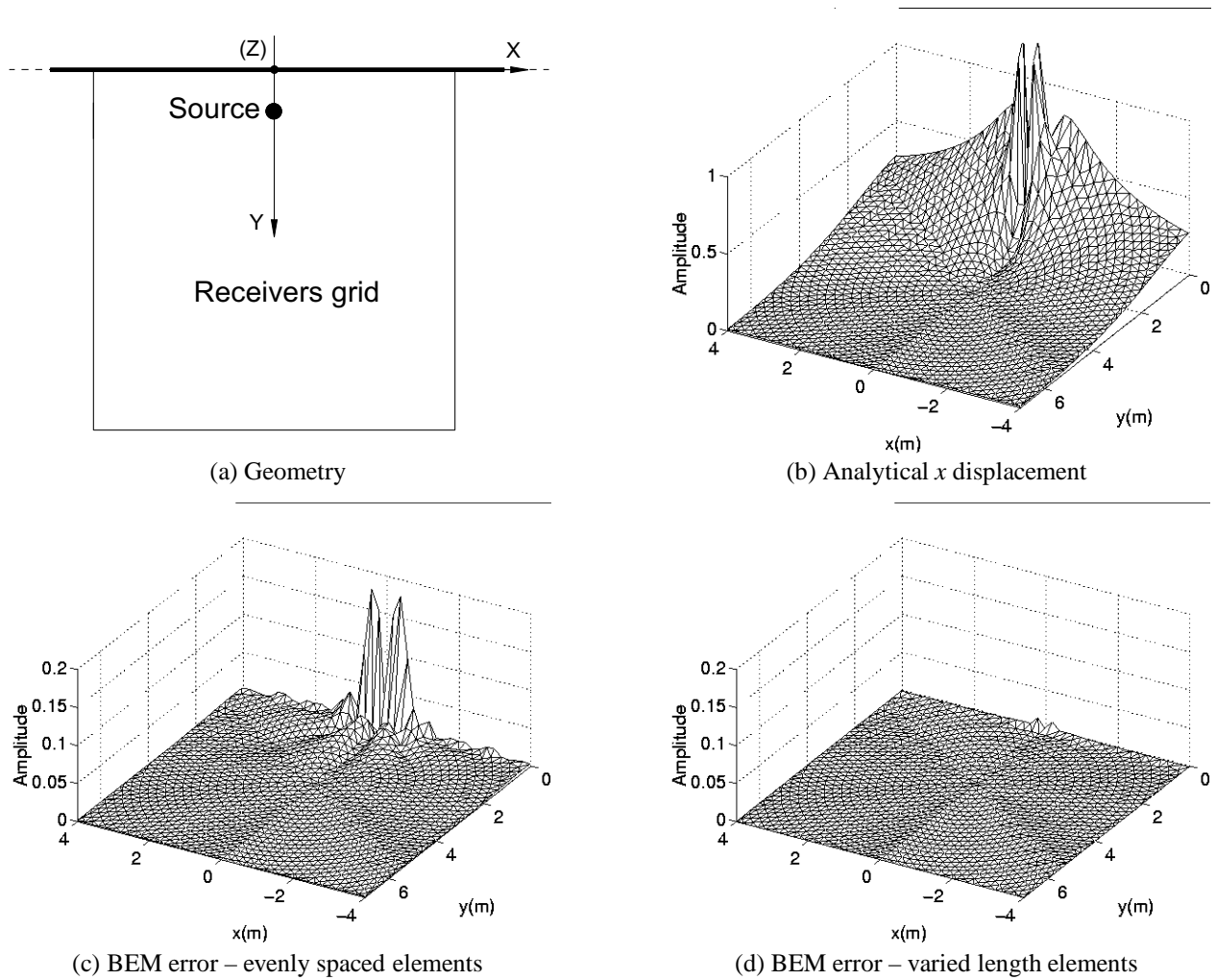


Figure 5 : Half-space problem validation.

with Δk_z , and $\Delta\omega$ being the wavenumber and frequency steps, respectively [Bouchon and Aki (1977)]. The spatial separation L must be large enough for contamination of the response by the periodic sources not to occur. Thus, the contribution to the response by the fictitious sources must occur at times later than T . It is also very useful for this if the frequency axis is shifted slightly downward, by considering complex frequencies with a small imaginary part of the form $\omega_c = \omega - i\eta$ (with $\eta = 0.7\Delta\omega$). The periodic sources are thus practically eliminated. In the time domain, this shift is later taken into account by applying an exponential window $e^{\eta t}$ to the response [Kausel (1992)].

5 Numerical applications

Selected results are presented for simulations with three simple geometries: a flat surface, a smooth ridge and a smooth

canyon. The ridge and the canyon deformations were defined with circular arcs of constant radius (2.0 m), (see Fig. 6). At time $t = 0$, a point source, defined by the dilatational potential ϕ , expressed as shown in Eq. 1, acts at the coordinates $(x = -15.0 \text{ m}, y = 0.5 \text{ m}, z = 0.0 \text{ m})$, creating a spherical dilatational pulse propagating away from it.

The dilatational wave velocity ($\alpha = 4208 \text{ m/s}$), the shear wave velocity ($\beta = 2656 \text{ m/s}$) and density ($\rho = 2140 \text{ Kg/m}^3$) of the elastic medium remain constant in all the analyses. Computations are performed in the frequency range (40 – 1280 Hz), with a frequency increment of 40.0 Hz, which determines the total duration ($T = 25.0 \text{ ms}$) of the analysis in the time domain. The source time dependence is a Ricker wavelet with a characteristic frequency of 450 Hz.

The field generated is computed at two lines of 41, evenly spaced (0.25 m), receivers. One of the lines of receivers is

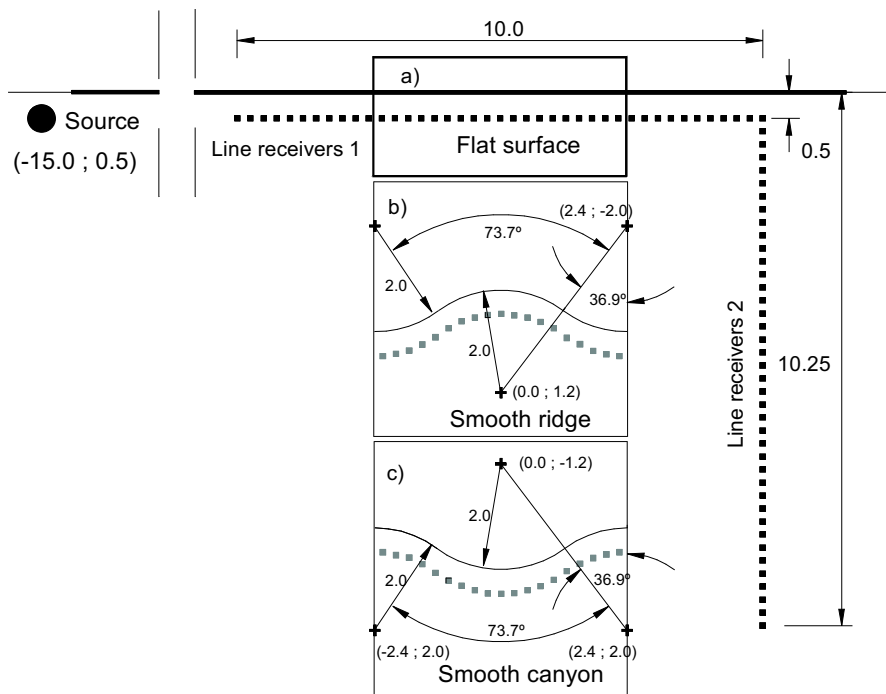


Figure 6 : Geometry for numerical applications.

placed horizontally 0.5 m below the surface (line 1), while the second is placed vertically at $x = 5.0$ m (line 2).

The surface topographies are modeled with a number of linear boundary elements that changes with the excitation frequency of the harmonic load. The ratio between the wavelength of the incident waves and the length of the boundary elements is kept to a minimum of 6. In any case the number of the boundary elements used to model each surface is never less than 23.

Simulations are performed following waves with different apparent wave velocities along the z axis to quantitatively study the 3D effects of the scattering. This apparent wave velocity (c) results from waves arriving at the z axis with a path inclination given by $\arccos(v/c)$, where v is the true wave velocity (see Fig. 7). In the equations presented above k_z is taken to be ω/c . In the examples selected, three apparent velocities (c) are chosen, namely $c = \infty$ m/s, $c = 4208$ m/s and $c = 2656$ m/s. Waves arriving at the receivers by $c = \infty$ m/s, which can be understood as a pure two-dimensional problem where the source is linear. As the path inclination ranges from 90° to 0° , there is a lower bound value for c that corresponds to the slowest wave velocities (Rayleigh waves). Below this value, there are inhomogeneous waves which decay very quickly with decreasing values of c .

As the P waves impinge on the surface, they scatter back into the medium as P and S waves (the latter as a result of P - S conversion). In addition, there are guided waves – Rayleigh waves

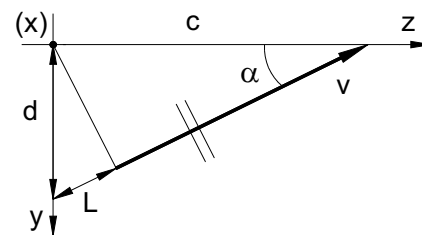


Figure 7 : Apparent wave velocity.

– propagating along the surface, which decay very rapidly with the distance to its surface.

Figure 8-10 display the amplitude of the total horizontal (x) displacement time and the space-frequency responses recorded at the receivers placed along line 1, for the three topographical surfaces. Lines indicating the limits of the topographical deformations and their inflection points (locating the change of curvature from convex to concave) are added to allow an easier interpretation of the results.

When $c = \infty$ m/s (Fig. 8), and the surface is flat, the first set of pulses recorded at the receivers corresponds to the incident P field and P waves reflected from the surface, while second arrivals are S mode converted waves resulting from the P wave incidence on the surface. The guided waves (R) follow the S waves, but given the small difference in velocities, they do not

fully separate as two pulses. The different pulses are identified in this figure with the labels P , S and R . The arrival times obtained for the different pulses are consistent with the predictions given by ray acoustics.

The results obtained when the topographical surface is irregular reveal a significant interference that increases with frequency. In the case of the smooth ridge, complicated wave patterns are caused by reverberations within the concave part of the surface. The space-frequency response agrees with this interpretation, locating a more pronounced wave field difference close to the central part of the line receivers. It can be further observed that the time responses show signal amplification and de-amplification at those same receivers. In the case of the smooth canyon, amplification of the signal occurs, but here it is close to the extreme of the deformation, again within the concave parts of the surfaces. The space-frequency response places amplifications of the signal at those same receivers. As expected, higher responses occur at the edge nearer to the dynamic source. The presence of the ridge and the canyon causes a “shadow” after the deformations, which is more pronounced in the case of a canyon.

As the apparent velocity decreases, both the arrival times of the different pulses and their amplitude decrease (see Fig. 9-10), indicating that the scattering energy is mainly concentrated in the vertical z plane containing the dynamic source. A pulse in these plots, with a travel time τ , corresponds to waves that travel from the source to the reflector and back to the receiver, along the same ray path inclination in relation to the z axis. The travel distance (L) in this domain is smaller because it corresponds to the projection of the initial vertical path (d) relative to the inclined path, leading to a distance $L = d \sin[\arccos(v/c)]$ (see Fig. 7). In this way, a fall in the apparent velocity causes a better separation of the P , S and Rayleigh waves. When the apparent velocity equals the velocity of the P waves (see Fig. 9), the waves traveling at this velocity arrive at the various receivers at $t = 0.0$ ms, and only the waves traveling at lower velocity, the S and Rayleigh waves, survive in these time plots. Furthermore, when the apparent velocity is assumed to be $c = 2656$ m/s, only the guided waves (Rayleigh waves) survive.

The concave parts of the surface determine the position of the amplification signals. However, interference from the different topographic deformations decreases as the apparent wave velocity along z diminishes. It can be further observed that the amplitude of the Rayleigh waves decays with the distance to the source (see Fig. 10).

Figure 11 illustrates the vertical displacement at the receivers, again placed along line 1, when the apparent velocity is assumed to be $c = \infty$ m/s. Given the position of the source close to the surface, receivers placed in the vicinity of this surface are mostly submitted to horizontal P displacement, so the P waves decrease in importance, as shown in this figure. Again, as shorter incident waves are excited, i.e. as the frequency in-

creases, the scattered field exhibits wave pattern interference similar to that found for the horizontal wave displacement: amplification of the signal occurs at concave parts of the topographical surfaces. In fact, the space-frequency responses for the smooth canyon and the ridge denote differences in relation to the wave field calculated for the flat surface, which agrees with this behavior. As the apparent velocity decreases, the interference from the different topographical deformations rapidly loses its importance (not illustrated). As expected, the vertical displacement of the Rayleigh waves is larger than its x displacement.

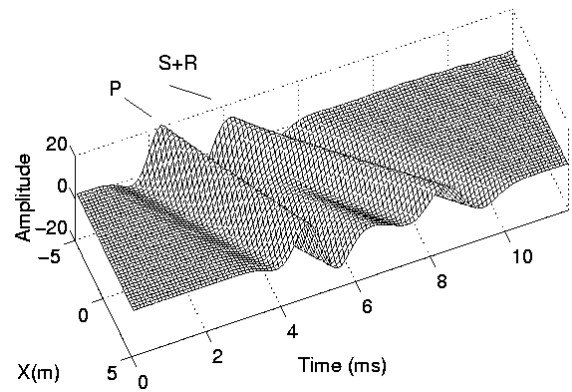
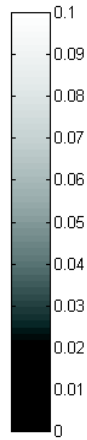
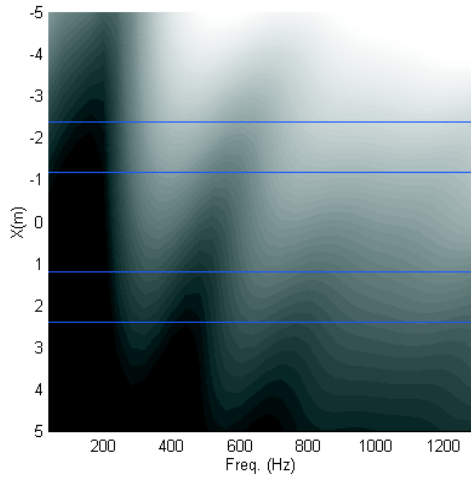
The z displacement is null for $c = \infty$ m/s, which corresponds to the two dimensional field. Figure 12 shows the z displacement at receivers, again placed along line 1, when the apparent velocity is assumed to be $c = 4208$ m/s. The type of topographical surface is still important. As the frequency increases, the space-frequency domain still shows higher amplitude scattered responses in the vicinity of the concave part of the surface deformations.

Figures 13-14 display the total displacement time recorded at the receivers placed along line 2, for the three topographical surfaces. Figure 13a depicts the horizontal (x) displacement when the apparent velocity is $c = \infty$ m/s. The result of the incident pulse P and P reflected pulse from the surface is labeled P , while the S mode converted pulse resulting from the P incidence pulse on the surface and the Rayleigh pulse are labeled S and R , respectively. The flight time of each of these pulses corresponds to the travel path of a pulse from the source to the surface and back to the receivers.

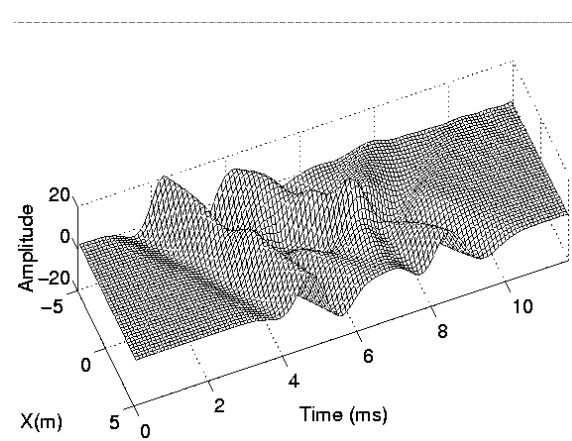
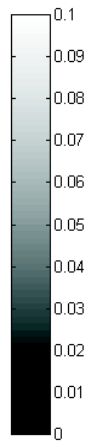
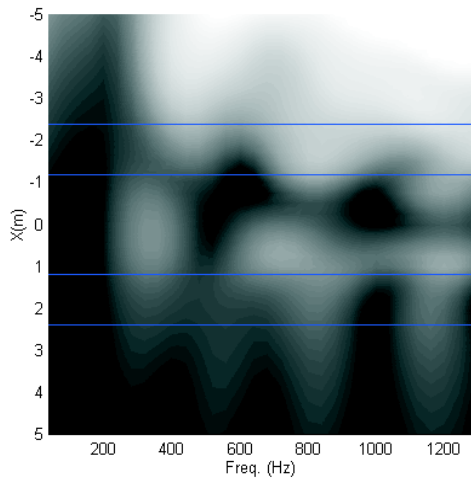
Analysis of the results reveals complicated wave patterns, which originate in reverberations within the topographical surface deformation. Additional pulses are present. The pulse that reflects on the surface topographical deformation as an S pulse is identified as S_2 .

The pulses directly incident on the canyon deformation are easily reflected onto the formation, creating a shadow behind the surface deformation. The time responses reveal this phenomenon, exhibiting body pulses with very small amplitude at an intermediate depth. Notice that the response increases again for receivers located at greater depths, owing to the reflection directed from the canyon surface. The only significant pulses surviving at the receivers close to the surface are those resulting from the guided modes, which decrease rapidly with depth. The results further show that these guided waves are more pronounced in the presence of the canyon than in the presence of the ridge.

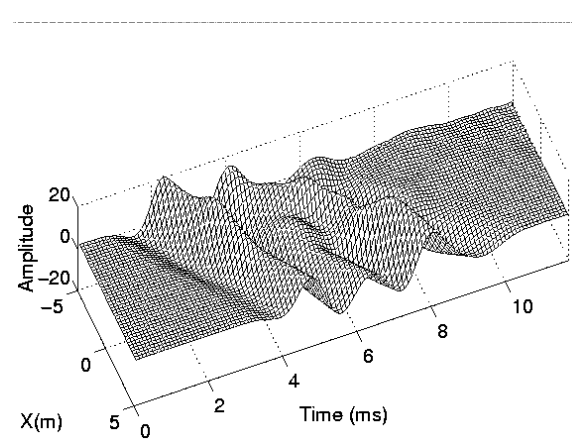
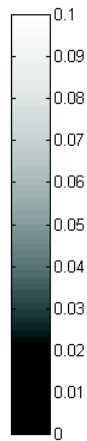
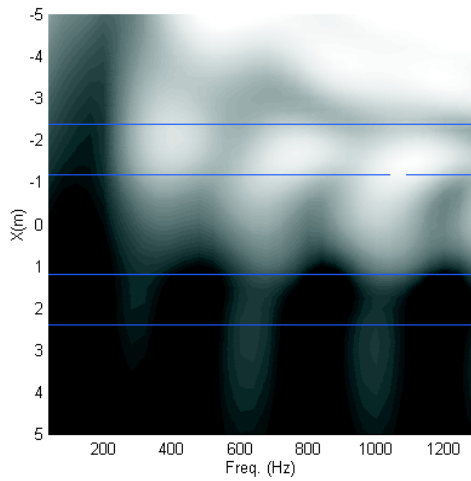
Figure 13b illustrates the horizontal displacement (x) when the apparent velocity is assumed to be $c = 4208$ m/s (velocity of the P waves). As explained before, only the waves with velocity less than that of the P wave remain (S and Rayleigh waves). The amplitude of this remaining wave field diminishes and the effect of the shadow phenomenon is significantly reduced.



Flat surface



Smooth ridge



Smooth canyon

Figure 8 : Total horizontal displacement time and frequency responses recorded at the receivers placed along line 1: $c = \infty$ m/s.

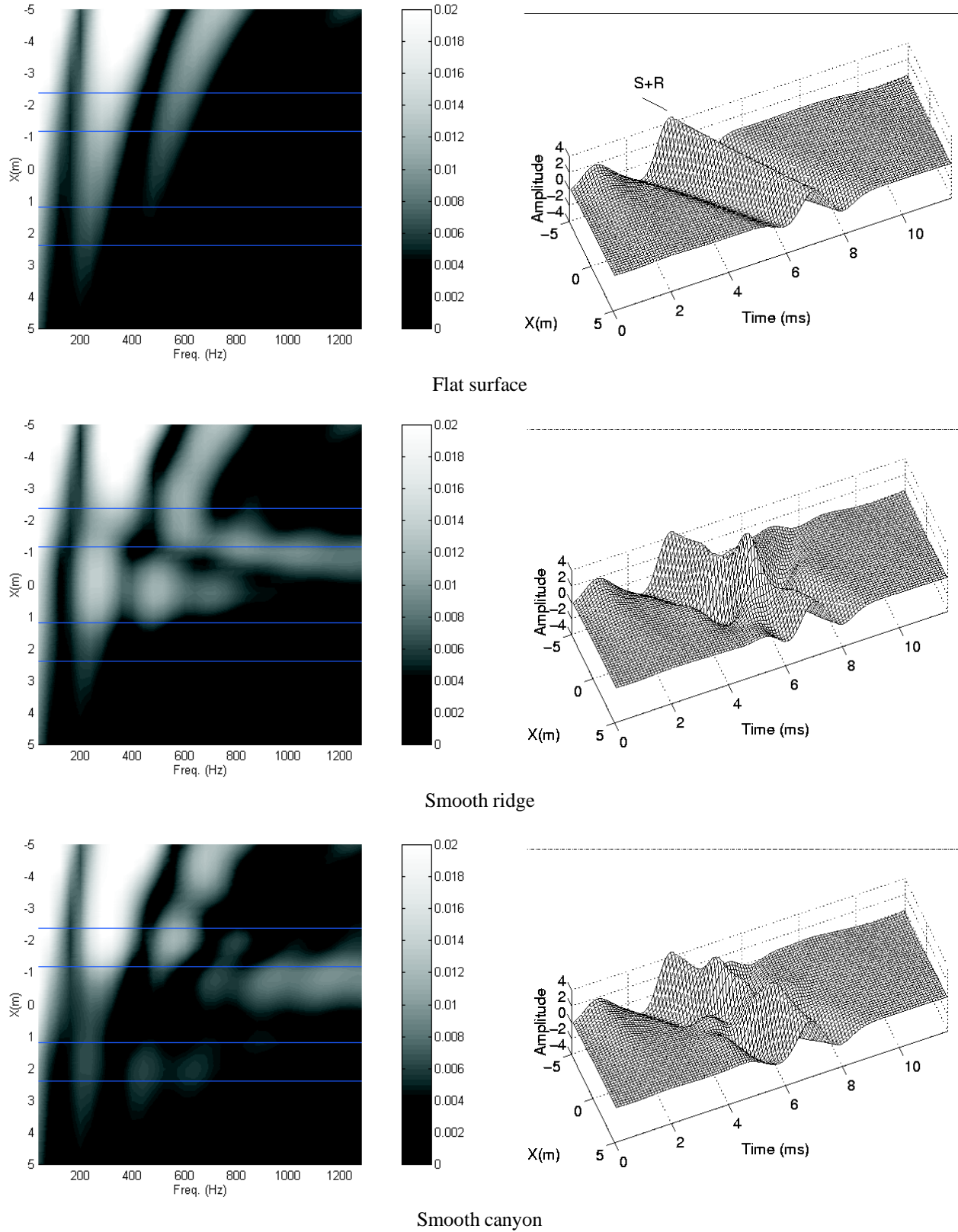


Figure 9 : Total horizontal displacement time and frequency responses recorded at the receivers placed along line 1: $c = 4208 \text{ m/s}$.

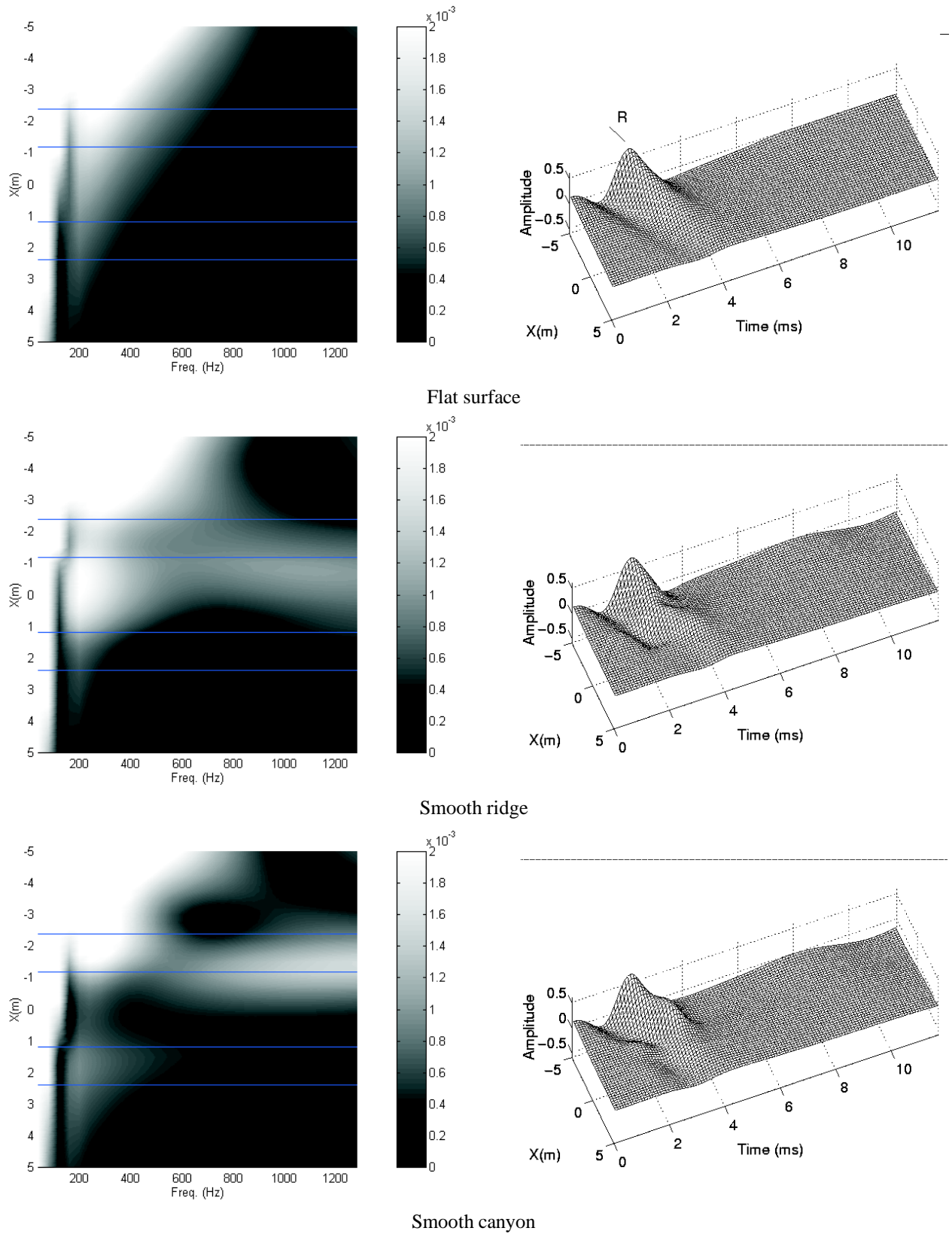


Figure 10 : Total horizontal displacement time and frequency responses recorded at the receivers placed along line 1: $c = 2656 \text{ m/s}$.

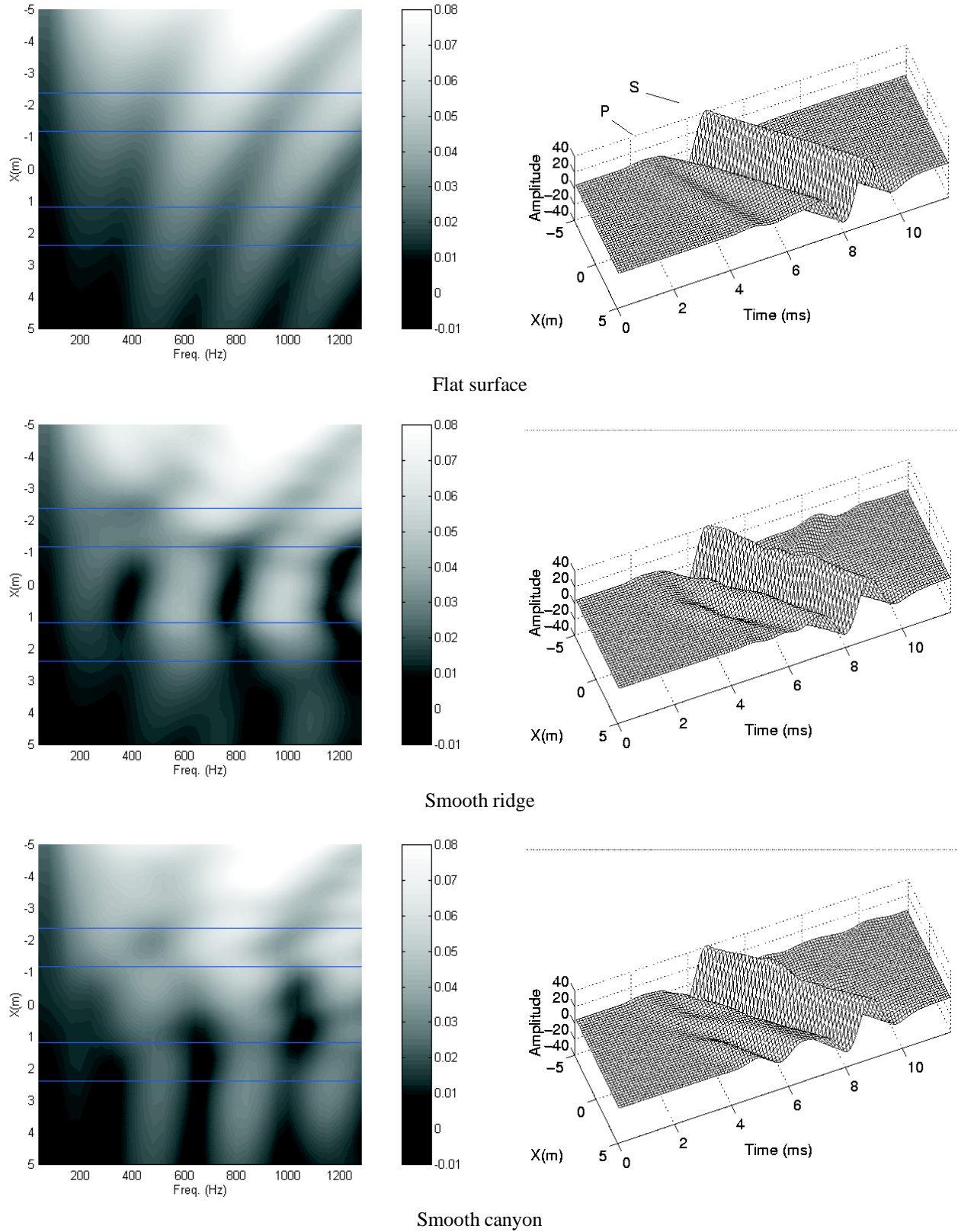


Figure 11 : Total vertical displacement time and frequency responses recorded at the receivers placed along line 1: $c = \infty$ m/s.

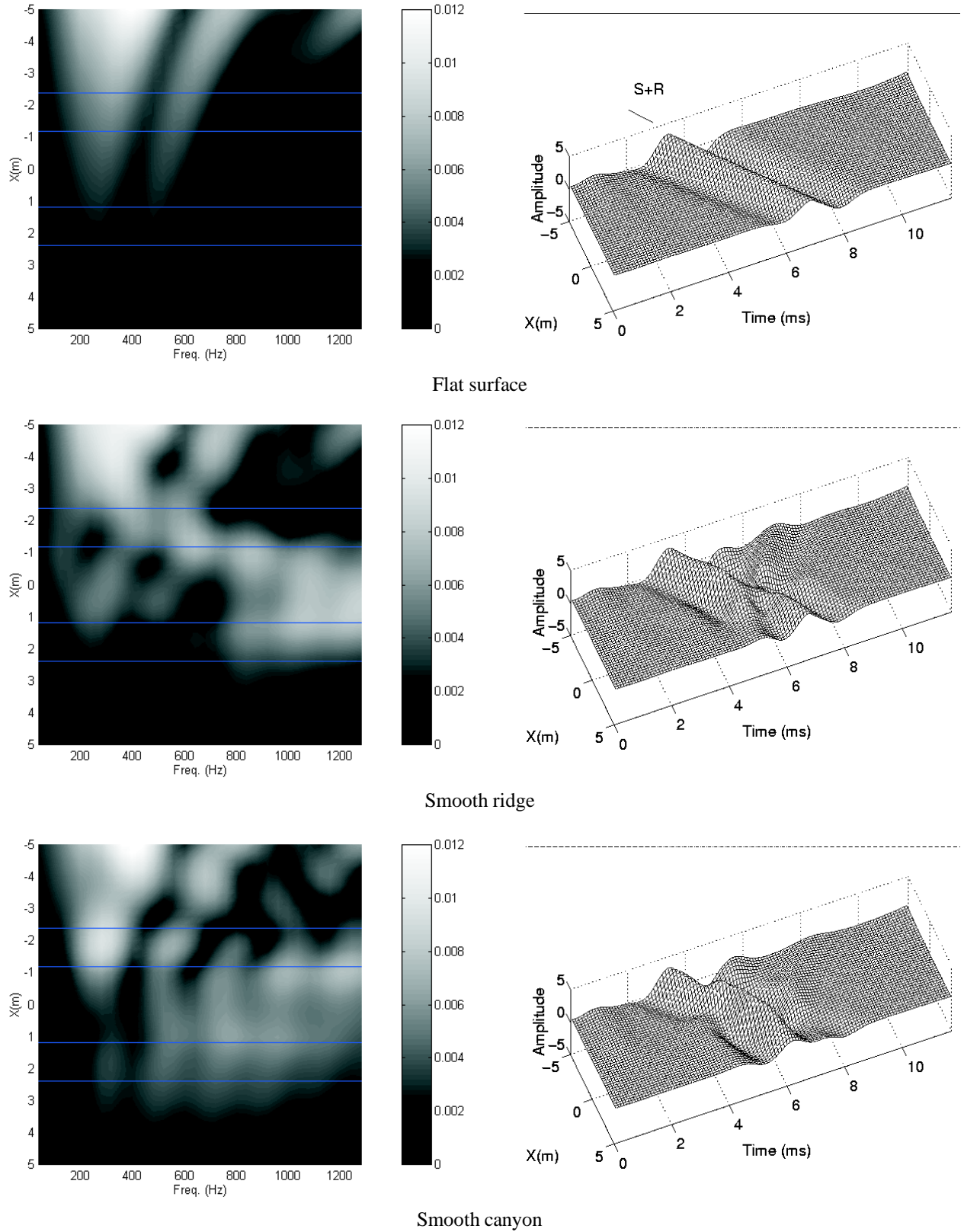


Figure 12 : Total z displacement time and frequency responses recorded at the receivers placed along line 1: $c = 4208$ m/s.

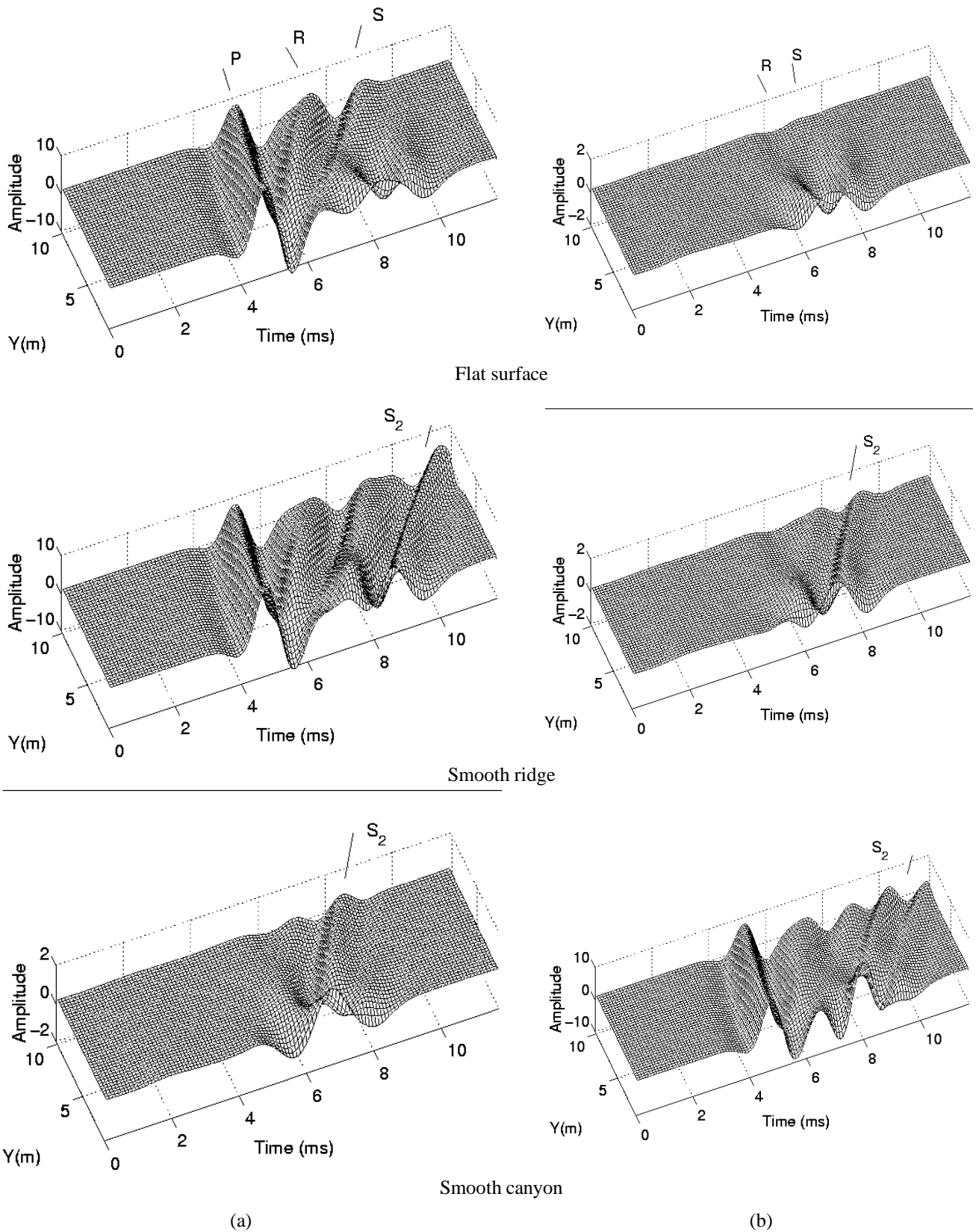
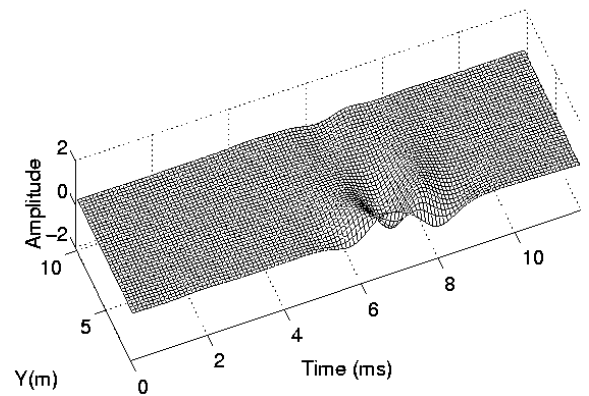
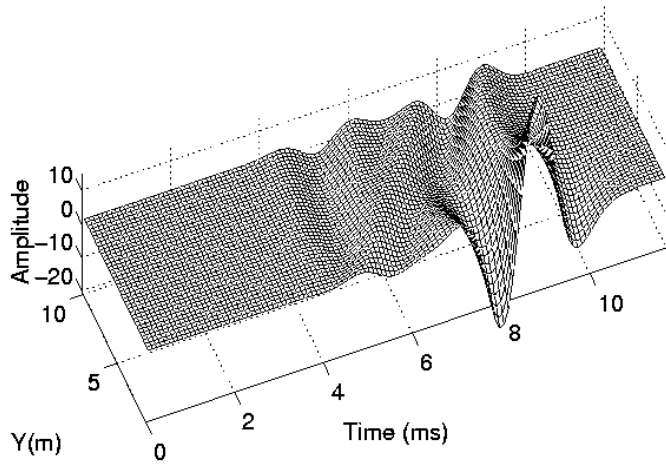
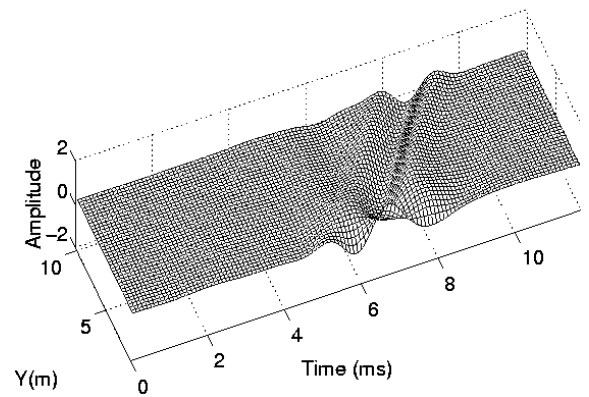
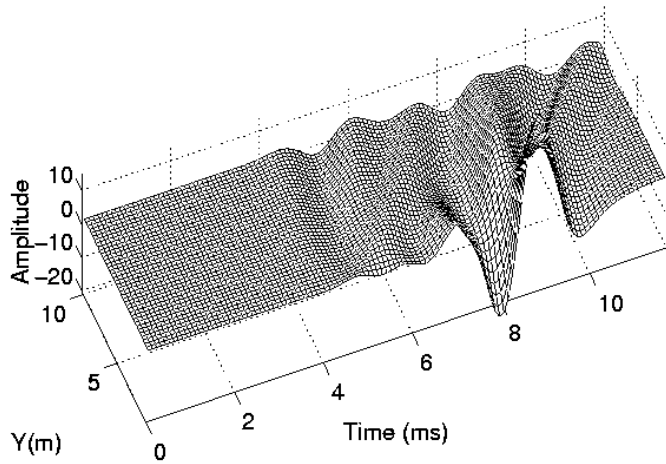


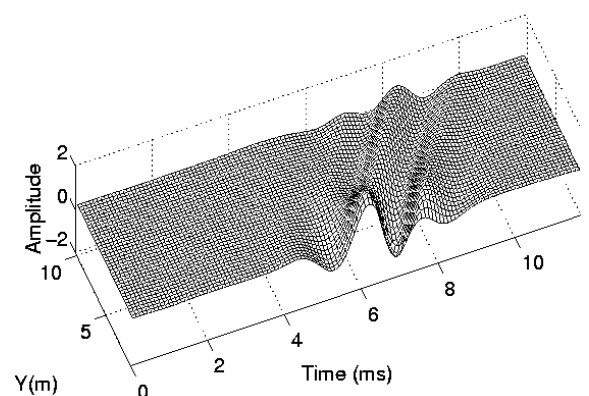
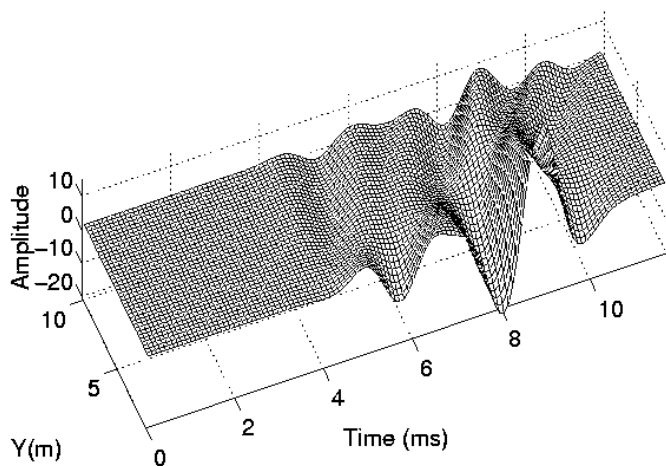
Figure 13 : Total horizontal displacement time responses recorded at the receivers placed along line 2: a) $c = \infty$ m/s, b) $c = 4208$ m/s.



Flat surface



Smooth ridge



Smooth canyon

(a)

(b)

Figure 14 : Time responses recorded at the receivers placed along line 2: a) Total vertical displacements when $c = \infty$ m/s, b) Total z displacements when $c = 4208$ m/s.

The vertical displacement time (y) for the apparent velocity $c = \infty$ m/s, is plotted in Fig. 14a. It can be observed that the amplitude of the wave field is higher than for the horizontal displacement. Nevertheless, as before, the P waves lose their importance and the influence of the topographic deformation is still present.

Figure 14b displays the z displacement for the apparent velocity $c = 4208$ m/s. The time response follows a behavior similar to that observed in the (x) direction. Again, the results show that the amplitude of the guided waves is more pronounced in the presence of the canyon.

6 Conclusions

The boundary element formulation developed was found to be efficient in the calculation of the 3D scattered field generated by a dilatational point load illuminating a half-space with topographical deformations. It could therefore be used in the context of research on seismic problems.

This program was used to compute the wave fields in the vicinity of smooth ridges and canyons in homogeneous elastic media when they are illuminated by dilatational point sources. The frequency and synthetic seismograms were built following waves with different apparent wave velocities along the z axis. The time responses appear very complicated but were consistent with the predictions given by ray acoustics, and were used by the authors to elucidate the most important aspects, with an eye to developing non-destructive testing and imaging methods.

The bigger interference noted in the time and frequency responses, when we move from the flat half-space and include the smooth ridge and canyon deformations, originate within the concave parts of the surface deformations, leading to the amplification and de-amplification of the signals. As the apparent velocity decreases, the arrival times of the different pulses and their amplitude both decrease, indicating that the scattering energy is mainly concentrated in the vertical z plane containing the dynamic source. It can be further observed that the direct incident pulses on the canyon deformation are easily reflected onto the formation, creating a shadow behind the surface deformation.

References

- Banerjee, P. K.** (1994): *The Boundary Element Methods in Engineering*. McGraw-Hill Book Company.
- Bard, P. Y.; Tucker, E. T.** (1985): Underground and the ridge site effects: a comparison of observation and theory. *Bulletin of the Seismological Society of America*, vol. 75, pp. 905–922.
- Bouchon, M.** (1985): A simple, complete numerical solution to the problem of diffraction of sh waves by an irregular surface. *J. Acoust. Soc. Am.*, vol. 77, pp. 1–5.
- Bouchon, M.; Aki, K.** (1977): Discrete wave-number representation of seismic-source wave field. *Bull. Seism. Soc. Am.*, vol. 67, pp. 259–277.
- Brebbia, C. A.; Telles, J. C. F.; Wrobel, L. C.** (1984): *Boundary Elements Techniques*. Springer-Verlag, Berlin Heidelberg New York, Tokyo.
- Datta, S. K.; Shah, A. H.** (1982): Scattering of sh-waves by embedded cavities. *Wave Motion*, vol. 4, pp. 265–283.
- Davis, L. L.; West, L. R.** (1973): Observed effects of topography on ground motion. *Bulletin of the Seismological Society of America*, vol. 63, pp. 283–298.
- Geli, L. L.; Bard, P. Y.; Jullien, B.** (1988): The effect of topography on earthquake ground motion: a review and new results. *Bulletin of the Seismological Society of America*, vol. 78, pp. 42–63.
- Griffiths, D. W.; Bollinger, G. A.** (1979): The effect of appalachian mountain topography on seismic waves. *Bulletin of the Seismological Society of America*, vol. 69, pp. 1081–1105.
- Kausel, E.** (1974): *Forced vibrations of circular foundations in layered media*. MIT Research Report 70-3, Department of Civil Engineering, Massachusetts Institute of Technology, Cambridge, MA, USA.
- Kausel, E.; Roesset, J. M.** (1992): Frequency domain analysis of undamped systems. *Journal of Engineering Mechanics, ASCE*, vol. 118, no. 4, pp. 721–734.
- Kawase, H.** (1988): Time-domain response of a semicircular canyon for incident sv, p and rayleigh waves calculated by the discrete wavenumber boundary element method. *Bulletin of the Seismological Society of America*, vol. 78, pp. 1415–1437.
- Lee, V. W.** (1977): On deformations near circular underground cavity subjected to incident plane sh waves. In *Symp. of Appl. Computer Methods in Eng.*, pp. 951–961. Univ. of Southern California, Los Angeles.
- Lee, V. W.** (1988): Three-dimensional diffraction of elastic waves by a spherical cavity in an elastic half-space. 1: Closed-form solutions. *Soil Dyn. Earthq. Eng.*, vol. 7, pp. 149–161.
- Lee, V. W.; Cao, H.** (1989): Diffraction of sv waves by circular canyons of various depths. *J. Eng. Mec. - Am. Soc. Civil Eng.*, vol. 115, pp. 2035–2056.
- Lee, V. W.; Karl, J. A.** (1992): Diffraction of sv waves by underground circular cylindrical cavities. *Soil Dyn. Earthq. Eng.*, vol. 11, pp. 445–456.
- Lee, V. W.; Wu, X.** (1994): Application of the weighted residual method to diffraction by 2-d canyons of arbitrary shape: Ii. incident p, sv and rayleigh waves. *Soil Dyn. Earthq. Eng.*, vol. 13, pp. 365–375.

- Luco, J. E.; Wong, H. L.; De Barros, F. C. P.** (1990): Three-dimensional response of a cylindrical canyon in a layered half-space. *Int. J. Earthquake Eng. Struct. Dyn.*, vol. 19, pp. 799–817.
- Lysmer, J.; Udaka, T.; Seed, H. B.; Hwang, R.** (1974): *LUSH - A computer program for complex response analysis of soil-structure systems*. Report No. EERC 74-4, Earthquake Engineering Research Center, University of California, Berkeley, CA, USA.
- Manolis, G.; Beskos, D.** (1988): *Boundary Element Methods in Elastodynamics*. Unwin Hyman (sold to Chapman and Hall), London.
- Moeen-Vaziri, N.; Trifunac, M. D.** (1988): Scattering and diffraction of plane p and sv waves by two-dimensional inhomogeneities: Part ii. *Soil Dyn. Earthq. Eng.*, vol. 7, pp. 189–200.
- Ohtsuki, A.; Harumi, K.** (1983): Effect of topography and subsurface inhomogeneities on seismic sv waves. *Earthq. Eng Struct. Dyn.*, vol. 11, pp. 441–462.
- Pao, Y. H.; Mow, C. C.** (1973): *Diffraction of Elastic Waves and Dynamic Stress Concentrations*. New York: Crane and Russak.
- Pedersen, H. A.; Sánchez-Sesma, F. J.; Campillo, M.** (1994): Three-dimensional scattering by two-dimensional topographies. *Bulletin of the Seismological Society of America*, vol. 84, pp. 1169–1183.
- Pei, D.; Papageorgiou, A. S.** (1993): Three-dimensional response of an infinitely long cylindrical canyon to obliquely incident seismic waves (abstract). *Seism. Res. Lett.*, vol. 64, pp. 27.
- Phinney, R. A.** (1965): Theoretical calculation of the spectrum of first arrivals in layered elastic mediums. *J. Geophys. Res.*, vol. 70, pp. 5107–5123.
- Sanchez-Sesma, F. J.** (1983): Diffraction of elastic waves by three dimensional surface irregularities. *Bull. Seism. Soc. Am.*, vol. 73, pp. 1621–1636.
- Sánchez-Sesma, F. J.** (1987): Site effects on strong ground motion. *Journal of Soil Dynamics and Earthquake Engineering*, vol. 6, pp. 124–132.
- Sánchez-Sesma, F. J.; Campillo, N.** (1991): Diffraction of p, sv, and rayleigh waves by topographical features: a boundary integral formulation. *Bull. Seism. Soc. Am.*, vol. 81, pp. 2234–2253.
- Sánchez-Sesma, F. J.; Campillo, N.** (1993): Topographical effects for incident p, sv, and rayleigh waves. *Tectonophysics*, vol. 218, pp. 113–125.
- Sánchez-Sesma, F. J.; Rosenblueth, E.** (1979): Ground motion on alluvial valleys under incident plane sh waves. *Int. J. Earthquake Eng. Struct. Dyn.*, vol. 7, pp. 441–450.
- Shah, A. H.; Wong, K. C.; Datta, S. K.** (1982): Diffraction of plane sh waves in a half-space. *Earthq. Eng. and Struct. Dyn.*, vol. 10, pp. 519–528.
- Stamos, A. A.; Beskos, D. E.** (1996): 3-d seismic response analysis of long lined tunnels in half-space. *Journal of Soil Dynamics and Earthquake Engineering*, vol. 15, pp. 111–118.
- Tadeu, A. J. B.; Kausel, E.** (2000): Green's functions for two-and-a-half dimensional elastodynamic problems. *Journal of Engineering Mechanics, ASCE to appear*.
- Tadeu, A. J. B.; Santos, P. F. A.; Kausel, E.** (1999): Closed-form integration of singular terms for constant, linear and quadratic boundary elements -part i: Sh wave propagation. *EABE - Engineering Analysis with Boundary Elements*, vol. 23, no. 8, pp. 671–681.
- Tadeu, A. J. B.; Santos, P. F. A.; Kausel, E.** (1999): Closed-form integration of singular terms for constant, linear and quadratic boundary elements - part ii: Sv-p wave propagation. *EABE - Engineering Analysis with Boundary Elements*, vol. 23, no. 9, pp. 757–768.
- Todorovska, M. I.; Lee, V. W.** (1990): A note on response of shallow circular valleys to rayleigh waves: analytical approach. *Earthquake Eng. Vibration*, vol. 10, pp. 21–34.
- Todorovska, M. I.; Lee, V. W.** (1991): Surface motion of circular valleys of variable depth for incident plane sh waves. *Soil Dynamics Earthquake*, vol. 10, pp. 192–200.
- Trifunac, M. D.** (1971): Surface motion of a semi-cylindrical alluvial valley for incident plane sh waves. *Bull. Seism. Soc. Am.*, vol. 61, pp. 1755–1770.
- Trifunac, M. D.** (1973): Scattering of plane sh waves by a semi-cylindrical canyon. *Int. J. Earthquake Eng. Struct. Dyn.*, vol. 1, pp. 267–281.
- Waas, G.** (1972): *Linear two-dimensional analysis of soil dynamics problems in semi-infinite layered media*. PhD dissertation, University of California, Berkeley, CA, USA.
- Wong, H. L.** (1982): Effect of surface topography on the diffraction of p, sv, and rayleigh waves. *Bull. Seism. Soc. Am.*, vol. 72, pp. 1167–1183.
- Wong, H. L.; Jennings, P. C.** (1975): Effect of canyon topographies on strong ground motion. *Bull. Seism. Soc. Am.*, vol. 65, pp. 1239–1257.
- Wong, H. L.; Trifunac, M. D.** (1974): Surface motion of semi-elliptical alluvial valley for incident plane sh-waves. *Bull. Seism. Soc. Am.*, vol. 64, pp. 1389–1403.

Zhang, L.; Chopra, A. K. (1991): Three dimensional analyses of spatially varying ground motions around a uniform canyon in a homogeneous half-space. *Int. J. Earthquake Eng. Struct. Dyn.*, vol. 20, pp. 911–926.

